A New Frontal Instability: Theory and ERICA Observations

NATHAN PALDOR,* CHING-HWANG LIU, MICHAEL GHIL,† AND ROGER M. WAKIMOTO

Department of Atmospheric Sciences, University of California, Los Angeles, Los Angeles, California

(Manuscript received 16 March 1992, in final form 3 December 1993)

ABSTRACT

A short-wave instability theory is applied to secondary waves on a narrow cold-front rainband observed during the Experiment on Rapidly Intensifying Cyclones over the Atlantic (ERICA). The basic mean state is approximated by the parabolic, geostrophically balanced interface between two layers of homogeneous density. The observed wavelength of perturbations along the ERICA cold front is about 20–30 km and their doubling time is about 2 hours. The observed wavelength is well within the short-wave regime of the theory, which yields a growth rate in good agreement with the ERICA observations. The spatial patterns of both the horizontal and vertical velocity components observed during ERICA are consistent with the model-derived patterns.

1. Introduction

In recent years, frontal rainbands have been shown to accompany extratropical cyclones (Houze et al. 1976; Hobbs 1978; Houze and Hobbs 1982). One important type is the narrow cold-front rainband coincident with the position of the cold front. Hobbs and Biswas (1979) and James and Browning (1979) studied these cold-front rainbands and found a series of elliptic precipitation cores oriented at an angle of about 35° to the front. Hobbs and Parsons (1982) observed strong low-level convergence, strong updrafts, and high liquid water contents at the leading edge of the precipitation cores. Wang et al. (1983) found that the mean spacing between the bands was about 10–15 km, the top of the bands was at about 3–5 km, and the bands occupied an area between 50 and 200 km^2.

Several studies have examined the mechanisms controlling the formation of rainbands. Wang et al. (1983) suggested that the narrow wavelike rainbands embedded within wide cold-front rainbands are initiated by shear instability in the cold frontal zone. Wang and Hobbs (1983) studied the wavelike rainbands near the occluded surface front with a potentially unstable layer behind the nose of the cold front. They suggested that horizontal roll vortices in the boundary layer being reinforced by latent heat effects may provide a mechanism for rainband formation. A linear mathematical model was used to study this problem by Moore (1985). His result appeared to replicate these cold frontal rainbands. The most unstable wavelength was of approximately 15 km, and the time for the amplitude to double was about 8 min. This unstable wavelength is roughly consistent with that of the ERICA front, but the *e*-folding timescale is an order of magnitude smaller.

Parsons and Hobbs (1983b), on the other hand, reported on a regularly spaced train of rainbands with a length scale of 10–15 km that prevailed for nearly 2 h. This long life span implies that neither the genesis nor the eventual dissipation of these particular rainbands could have been associated with the onset of short-wave instabilities of Kelvin–Helmholtz type. It should be noted that Parsons and Hobbs (1983a) describe several situations in which the horizontal shear across the narrow, cold frontal rainband is eliminated (as a result of the interaction with a passing wide frontal rainband). In these instances, the organization of precipitation into cores along the front was eliminated. In those cases in which the shear across the front returned after interaction, the cores were observed to reform on a timescale of 10–75 min. Moore (1985) predicts growth rates comparable to the short end of this range (~10 min); his theory, however, does not adequately explain the longer timescales.

A different approach to the study of frontal evolution has been put forward by Paldor and Ghil (1990; hereafter PG). The basic idea underlying the PG approach has its origin in laboratory experiments on density fronts (Griffiths et al. 1982; GKS hereafter) and in the

* Permanent affiliation: Department of Atmospheric Sciences, The Hebrew University of Jerusalem, Jerusalem, Israel.

† Also affiliated with the Institute of Geophysics and Planetary Physics, UCLA.

Corresponding author address: Dr. Michael Ghil, Department of Atmospheric Sciences, 405 Hilgard Ave., Los Angeles, CA 90024-1565.

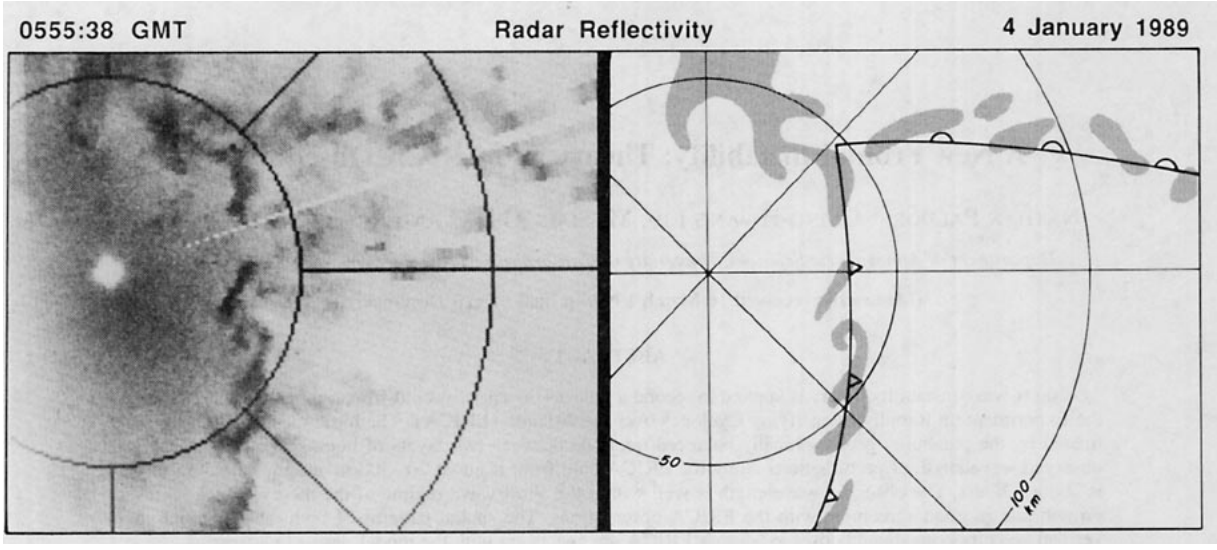

FIG. 1. The reflectivity pattern recorded by the P-3 lower-fuselage radar at 0555 UTC 4 January 1989. Left panel: gray area corresponds to reflectivity higher than 35 dBZ. Right panel: range marks are every 50 km. The schematic locations of the cold and warm fronts are superimposed on the simplified reflectivity pattern.

study of oceanic fronts (Paldor and Killworth 1987). The layered density profile in the basic state of these studies is geostrophically coupled with the velocity field, while the prescribed horizontal shear is such that the potential vorticity is finite even where the layer's thickness vanishes. A careful study of the phase speed of traveling waves perturbing the geostrophic basic state reveals complex phase speeds, that is, an exponential growth of selected perturbations. The calculated growth rate of these perturbations can then be compared with observations.

A simplifying assumption in the GKS- and PG-type frontal instability studies is that the atmosphere (or the ocean) is made up of two layers of slightly different densities and that the outcropping of the interface separating the two layers (along the so-called free streamline) models the location of the surface front. One of the layers is assumed to be initially motionless, while the second has a prescribed velocity field (see Fig. 3 in section 3). The two are coupled hydrostatically across the interface. Of particular interest is the coupled front, where the interface crops out along two parallel free streamlines; this configuration is unstable even when the initially motionless layer is infinitely thick so that no motion is generated there by the perturbations in the active layer (GKS, PG). A finite—though large—thickness of the initially motionless layer was shown by Paldor and Killworth (1987) to cause even faster growing perturbations to develop.

In both the infinitely deep and the very deep versions of the coupled front problem, the instabilities were essentially long waves, and beyond some finite wavenumber all perturbations had vanishingly small growth rates. By contrast, when the excess thickness of the passive over the active layer is initially very small, an "essentially short-wave" instability was found by PG. The growth rate of this instability increases linearly—for an inviscid fluid—with wavenumber. It is strongly dependent on the active layer reaching to over half of the total atmospheric height (see Fig. 3), that is, the passive layer aloft being thinner than the active layer near the ground. This model is, therefore, the one relevant to atmospheric fronts, where the active layer extends vertically to over half the troposphere's total thickness; moreover, since the perturbations' wavelength is much smaller than the front's length scale, the nondimensional wavenumber has to be—in some sense—large.

In this study, the aforementioned frontal instability theory is applied to data collected during the Experiment on Rapidly Intensifying Cyclones over the Atlantic (ERICA). In section 2, the ERICA observations are briefly reviewed. In section 3, the frontal instability theory is discussed and the growth rates calculated. The results are discussed in section 4. The rather complete observations of cold frontal structure during the ERICA experiment provide a good opportunity to evaluate the applicability of the PG theory to observed fronts, better than the typically scarce oceanic observations that motivated the earlier work or any other mesoscale atmospheric observations available until now.

2. Observations

The ERICA experiment was conducted from December 1988 to February 1989 (Hadlock and Kreitzberg 1988). Eight Intensive Observation Periods (IOPs) took place during this experiment and a variety

of data were collected, including conventional synoptic observations, surface observations, drifting-buoy, and dropsonde observations, and in situ measurements by the two NOAA P-3 aircraft. The P-3 aircraft are both equipped with two radars onboard: a C-band (5.59-cm wavelength) lower-fuselage radar and an X-band (3.22-cm wavelength) tail radar. The lower-fuselage radar performs only surveillance scans and records reflectivity. The tail radar scans in a 360° plane perpendicular to the aircraft ground track and records both reflectivity and velocity.

During IOP 4, a cyclone dramatically deepened over the ocean while a comprehensive dataset was being collected. The low center pressure was 994 mb at 0000 UTC 4 January and reached 938 mb at 0000 UTC 5 January, a drop of more than 50 mb in 24 h (Wakimoto et al. 1992). Five flight missions were deployed during IOP 4. During flights 1 and 2, the P-3 aircraft penetrated the cold front around 0400 UTC and 0600 UTC 4 January and made in situ measurements of the wind and thermodynamic properties on both sides of the front. At the same time the lower-fuselage radar detected wave-type precipitation cores along the cold front. This kind of precipitation structure was similar to that documented by Hobbs and Biswas (1979). From the reflectivity pattern at 0555 UTC the measured wavelength was determined to be about 20–30 km (Fig. 1).

The various observations during IOP 4 that were used to determine the position of the front as well as its structure were carried out over a period of several hours. We take them to be a snapshot of the front for want of any better means of obtaining such snapshots and because there is no indication of rapid changes in the frontal configuration over this time interval.

The position of the front was determined independently from three types of data, all yielding the same position. The wind measurements indicated the frontal position by the abrupt change in the wind direction, while the equivalent potential temperature sections yielded the frontal profile as the steepest gradient region (Fig. 2). These determinations were supplemented by horizontal cross sections of radar reflectivity (Fig. 1).

3. Theoretical and observed growth rate

a. Determination of the basic state

To verify the PG model's applicability to the observed phenomena, we have to determine whether the synoptic-scale frontal structure corresponds to the basic state assumed in the model. The PG model (Fig. 3) assumes a basic state comprising an active layer, where the alongfront velocity component (north–south in the case of the ERICA front) is large, and a passive layer where the velocity is due only to perturbations. The model assumptions of geostrophic balance and zero potential vorticity flow in the active layer result in a parabolic profile of the interface separating the two layers. The equivalent potential temperature section of Neiman et al. (1991, Fig. 7) was adapted here as Fig. 2a (see also Neiman et al. 1993). The section shows clearly that the ERICA front was characterized by such parabolic density profiles: nearby equivalent potential temperature profiles were very similar to that shown in Fig. 2a. The passive layer in the PG model occupies the entire height of the troposphere to the east of the surface front, while the active layer extends to over half this height only. Thus, as is evident from Fig. 3, the passive layer overlies the active one by filling the space between the top of the latter and the tropopause.

The mean tangential velocity in the active (heavy, cold) section of the front should decrease linearly away from the front in order for the PG model to apply; the normal velocity there, as well as both velocity components in the passive layer, should all vanish in the basic state. The observed alongfront velocity component is in fact, rather irregular in both the passive and active layers (Fig. 2b). The sharp jump observed across the front, however, dominates the picture and is consistent with the inferred basic state exhibiting a large northerly geostrophic velocity of 25 m s^{-1}, as dictated by the sloping interface (Fig. 2a).

Evidently, the velocity in the passive layer and the normal velocity in the active layer are not zero. It is reasonable, however, to treat these nonzero velocity components as well as the deviations of the tangential velocity from strict linearity as secondary to the basic structure; they could be due to nonuniform advancement of the front, on one hand, and to smaller-scale turbulence (Stull 1988), on the other. These ageostrophic velocities also mask the linear decrease of the geostrophic velocity westward, away from the front: over the distance of 45 km to the west of the front, where velocity measurements are available (Fig. 2b), the PG model predicts a drop in velocity of 4 m s^{-1} or less; such a drop is too small to be detected unambiguously in the observed velocity profile, given the highly erratic measurements at hand.

The third and last qualitative point to consider, before attempting a quantitative comparison between theory and observations, is the application of the coupled density front model of PG to the single ERICA front. It is a simple matter to consider only one-half of PG's parabolic profile and mirror image this half-parabola with respect to its apex. In fact, in the complementary problem where a vertical wall (a coast in the ocean context) is placed at the axis of symmetry, Paldor and Ghil (1991) found even stronger instabilities, their growth rate still increasing linearly with wavenumber in the short-wave regime.

Quantitative aspects of the basic state are determined as follows. The timescale in the PG theory is $1/f$ (where f is the Coriolis parameter), which at 35°N—where ERICA was carried out—is 200 min. The theo-

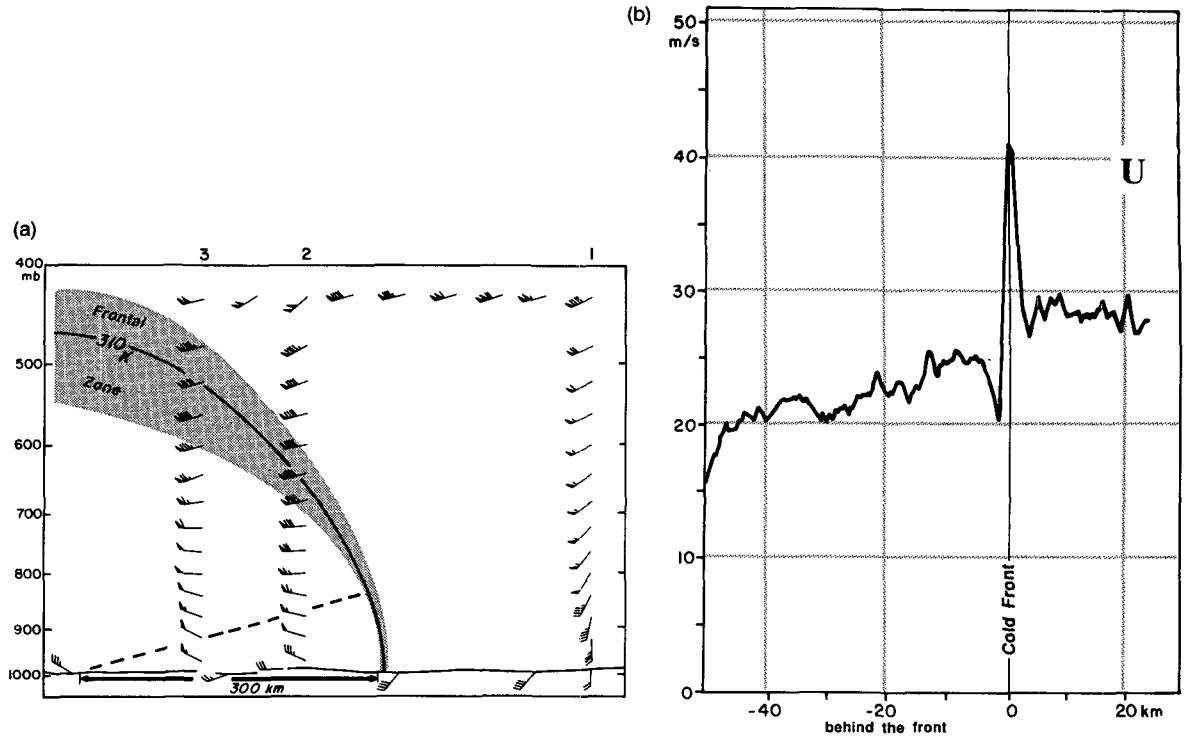

FIG. 2. The E–W vertical cross section through the cold front converted to UTC 0600 (based on Fig. 7 of Neiman et al. 1991). (a) The 310-K isopleth of equivalent potential temperature is highlighted and approximately represents the frontal location. Winds are derived from aircraft and dropsonde measurements (full bar is 5 m s^{-1}): dashed line is the theoretical velocity profile $U = f(y + 3 \cdot 10^5$ m), where U, f, and y are in SI units; this yields a northerly velocity of 25 m s^{-1} at the front. The numbers 1, 2, and 3 on the upper frame indicate the location of dropsondes 1, 2, and 3. The (across-front) y axis is the horizontal axis in both panels and it points east; its origin is chosen at the front. (b) A blowup of the observed profile of the alongfront velocity component U near the front. The wind is southerly on both sides of the front; the velocity jump encountered upon crossing the front from east to west is in approximate geostrophic balance with the sloping isentrope. This geostrophic jump at the front of nearly 25 m s^{-1} is $U(0)$, the basic state velocity of the PG model.

retical length scale is twice the horizontal distance between the intersection of the interface—chosen as the 310-K isentrope in the ERICA case—with sea level,

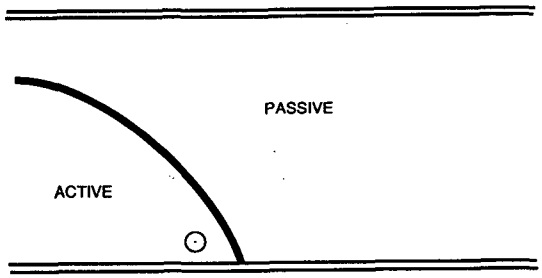

FIG. 3. Schematic diagram of the PG model geometry. In the mean state the tangential velocity in the active layer is in geostrophic balance with the sloping interface; all other velocity components vanish. As the slope of the interface decreases with distance from the point where it touches the surface, so does the tangential velocity. The active layer's maximum height occupies most of the total atmospheric height, with the passive layer over it filling the remaining space up to the tropopause. For details see Fig. 1 in PG.

on the one hand, and its apex—where the derivative of the profile vanishes—on the other. From Fig. 2a this distance is about 300 km, so that the length scale L equals 600 km.

An independent estimate of this length scale comes from the tangential shear, which should equal $f = 8.34 \times 10^{-5}$ s^{-1}. For the tangential velocity jump at the free streamline $U(0)$ (note that U is the alongfront mean velocity jump, which for the ERICA front is northerly) we get that the velocity vanishes at a distance of $L/2 = U(0)/f \doteq 300$ km from the free streamline. It follows that measurements of both velocity shear and interface variation support the estimate $L = 600$ km, chosen in the following. The velocity scale in PG is fL, which for the ERICA front equals 50 m s^{-1}. The nondimensional tangential velocity jump at the PG front is $1/2$, which corresponds to 25 m s^{-1}, very close to the observed value of $U(0)$.

The last (and hardest) quantity to be determined before the perturbation's growth is compared with the theory is the relative density difference $\Delta\rho/\rho$ between the active and passive layers. In the PG model the den-

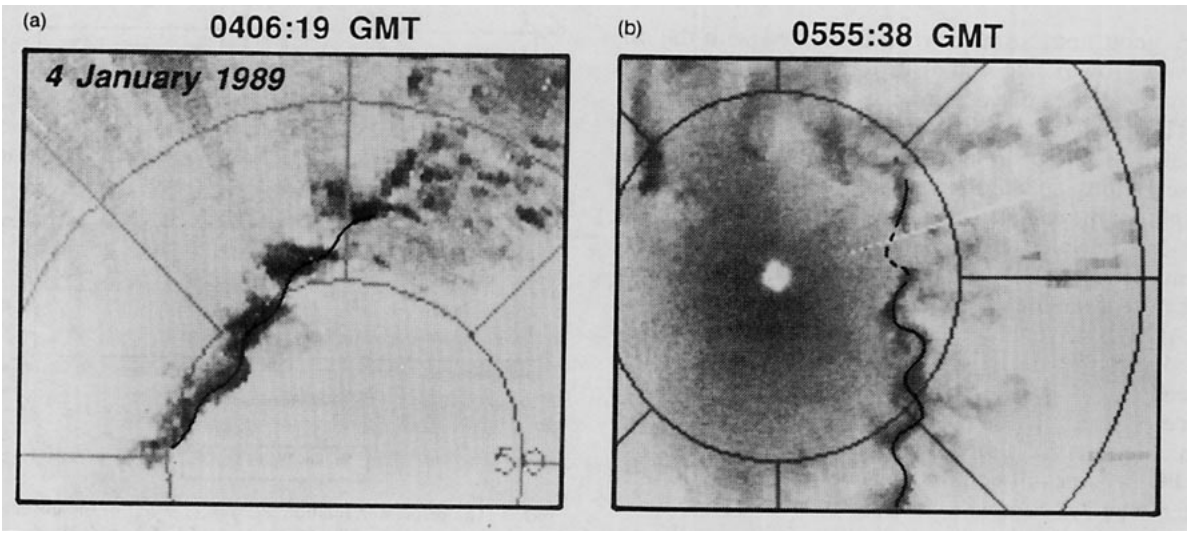

FIG. 4. A comparison between the wave structure of the rainband at (a) 0406 and (b) 0555 UTC. Panel (b) here is the same as the left panel in Fig. 1 and is repeated for comparison purposes. The increase in amplitude from about 3 km to about 6 km during this 2-h period is quite pronounced and is in good agreement with the growth rate of the PG theory.

sity in each of the layers is assumed constant with the active layer being, of course, heavier. In the ERICA observations, the density in each of the layers was first determined on the isobaric surfaces p = const by employing the thermodynamic relation for a perfect gas—$\rho = p/(RT_v)$, T_v being the virtual temperature and R the gas constant—and then averaging the density on all isobaric surfaces within each layer. The resulting value for the layer's density depends on the weighting used to reflect the larger mass of air at lower elevations in the active layer, as well as on the highest isobaric surface taken to lie within that layer.

Comparing the numbers from dropsondes 1 and 3 (see Fig. 2a) when using quadratic weighting,

$$(p - p_{\text{top}})^2/(p_{\text{surface}} - p_{\text{top}})^2, \quad \Delta\rho/\rho$$

is 5.3×10^{-3} for the data up to the 600-mb surface and 4.7×10^{-3} up to 650 mb. Linear weighting increases these numbers by about 25% while a uniform weighting yields values twice as large. The data from dropsondes 1 and 2 (with maximal height of 700 or 750 mb) yield estimates between 1 and 2 ($\times 10^{-3}$), so that the range of possible estimates for the relative density difference across the front is between 1 and 10 ($\times 10^{-3}$). The most plausible estimates are 4.7–5.3 ($\times 10^{-3}$), and we choose 5×10^{-3}, which yields a reduced gravity g' of 5×10^{-2} m s^{-2}.

The combination of the velocity scale of 50 m s^{-1} and the reduced gravity scale of 5×10^{-2} ms^{-2} yields a height scale $\bar{H} \equiv f^2L^2/g' \approx 50$ km. The maximal nondimensional height of the active layer in the PG theory is 1/8, which, according to the present scaling, corresponds to a maximal dimensional height of slightly over 6 km—in good agreement with the observed height of the 500 mb surface, namely, 5 km. The dimensional height scale of 50 km and the fact that the tropopause height across the ERICA system varied from 9 to 11 km yield a nondimensional total height r of the two layers combined between 0.18 and 0.22 (compare Fig. 3 here and Fig. 1 in PG; the total height in the latter is $r\bar{H}$).

Having determined the basic-state parameters of the theory for the ERICA front, we compare the theoretical growth rate with the observed one in the next subsection. The determination of the precise values of the basic-state parameters from given data is, obviously, not unique and other combinations cannot be ruled out. In addition to this inherent ambivalence, the dataset itself allows for a fairly wide latitude in pinning down each individual value.

b. Growth rate calculations

The observed wavelength of the perturbations along the ERICA IOP 4 cold front is on the order of 20–30 km (Figs. 1 and 4), which implies a nondimensional wavenumber of $k = 2\pi L/\lambda = 40\pi \sim 10^2$; the perturbations are thus undoubtedly short waves. In the original PG study, the short-wave instabilities were calculated for a total height of 0.15 and up to an alongfront wavenumber of 20. The values of the instability exponent are very sensitive to the nondimensional total height r: for $k = 20$ the exponent vanishes when r exceeds 0.2 (see Fig. 5 in PG). If we take the results of the PG study, where the instability exponents asymptote at a value of $0.02k$, and extrapolate these to the $k \sim 10^2$ value observed in IOP 4, we get a nondimensional e-folding time of 1/2, or about 100 min, at the latitude where ERICA was carried out. This is a

very good first estimate when compared with the observed growth rate and with the directly determined theoretical rates discussed next.

The growth rates of the PG-type instability were calculated for the parameter values applicable to ERICA observations and are presented in Fig. 5. The total height for the calculations shown in Fig. 5 is $r = 0.18$—the lowest value that is consistent with the observations. This value was chosen rather than a higher one because of the high sensitivity of the growth rates to it.

At high wavenumber values, the numerical method used to solve the eigenvalue problem for the phase speed c in PG had to be modified, because of the presence of $O(k^8)$ terms next to $O(1)$ terms in the 4×4 matching matrix. For $k \sim O(10^2)$, the matching used in PG becomes ill-conditioned. We therefore modified the method of computing the eigenvalues c, and hence the growth rates kc_i, by explicitly solving for the coefficients in three of the matching equations and varying c, so that the fourth equation be satisfied. This method proved applicable even at $k \sim O(10^2)$, where the PG requirement that the determinant of the matching matrix vanish failed to yield results.

The asymptotic nondimensional value of the instability exponent in Fig. 5 is $0.013k$. This is equivalent to a nondimensional e-folding time of 0.75, that is, about 2.5 h. From this estimate and the one of 1.5 h obtained by extrapolating directly the PG results to higher k, we conclude that the e-folding time for the evolution of the unstable perturbations with $k \approx 100$ on the IOP-4 front should be about 2 h.

This theoretical estimate is compared with observations as follows. During IOP 4, the P-3 aircraft penetrated the cold front at 0408 UTC in flight 1 (Fig. 4a) and at 0601 UTC in flight 2 (Fig. 4b), with the lower-fuselage radar recording the wave structure along the cold front; it is the latter perturbation that is shown in Fig. 1. The wavelength remained approximately the same during this 2-h period, but an increase in amplitude was noted at 0601 UTC (Figs. 4a,b). In addition to this amplitude increase, several hook features had developed at approximately 115° and 135° and 50 km, as seen in the radar picture of Fig. 1. By measuring the wave amplitude based on the lower-fuselage radar observations, we found that amplitudes at 0406 UTC and 0555 UTC were about 3 km and 6–7 km, respectively. This doubling during the 2-h interval matches well the growth-rate calculations presented above.

4. Spatial patterns and energetics

In the previous section it was shown that, using a mean state derived from the IOP-4 frontal structure, the growth rates of the PG theory fit the ERICA observations. We proceed in this section to analyze the spatial pattern of the perturbation velocity components observed across the ERICA front and compare them with the unstable eigenmodes of the PG theory.

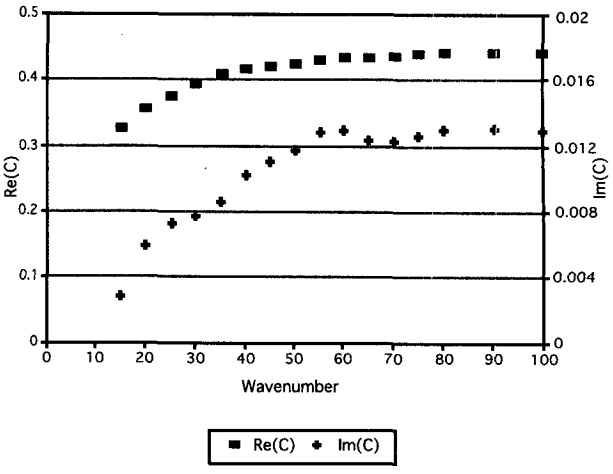

FIG. 5. The dispersion relation, $c(k) = c_r + ic_i$, of the unstable mode for a nondimensional total height $r = 0.18$.

a. Horizontal and vertical velocity

In the PG theory, the eigenfunctions within the active layer have the typical boundary-layer structure of solutions to a singular ordinary differential equation. Their amplitude attains its maximal value at the singular point (in this case the free streamline); it first decreases exponentially toward the interior and then begins to oscillate between (much smaller) positive and negative values. The rate of initial exponential decay and the number of zero crossings of the eigenfunction are strongly dependent on k—the *alongfront* wavenumber that appears as a parameter in the *cross-front* eigenvalue problem. An example of this structure is reproduced from PG in Fig. 6 here, where the active layer's (complex) alongfront perturbation velocity is shown as a function of the distance from the free streamline for a realistic total atmospheric height but for $k = 10$.

Direct calculation of the eigenfunctions for $k \sim O(10^2)$ is difficult, since the numerical scheme used in PG breaks down, as discussed in section 3b here. The modification of the scheme that produces the eigenvalues shown in Fig. 5 does not work as well for the eigenfunctions. Instead, we present in the appendix a WKB theory demonstrating that the spatial pattern shown in Fig. 6—with rapid exponential decay away from the free streamline—is the general one at $k \gg 1$. Both this theory and our experience with many eigenfunctions calculated for other values of wavenumber and total heights (not presented) show this to be the typical spatial pattern in all cases: an exponential decay away from the streamlines that becomes more rapid as k increases and an increase in the cross-frontal wavenumber of the oscillations. In the case of ERICA, where k is of the order of 100, the dimensional length scale

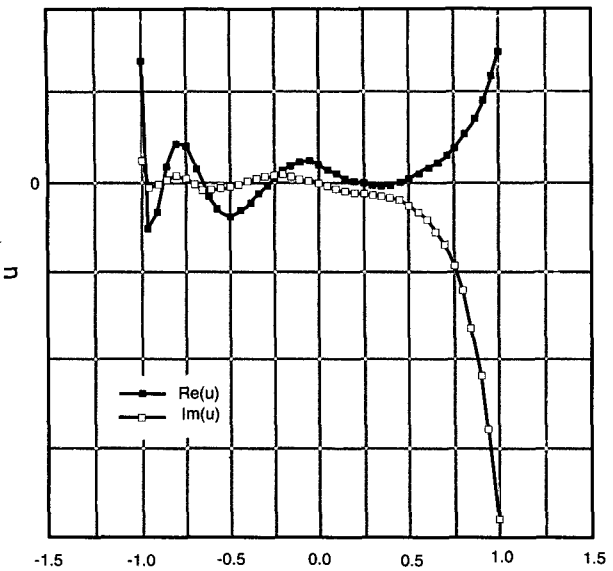

FIG. 6. The alongfront perturbation velocity u in the active layer as a function of the cross-front coordinate $y' = 2y + 1$ for $k = 10.0$ and total height of $r = 0.2$. Note that since the phase speed c (which is the eigenvalue in the PG stability problem) is complex, $c = c_r + ic_i$ (with $c_i \neq 0$ as the mode is unstable), so are the eigenfunctions. Hence, the phase of u, i.e., the relative values of $\mathrm{Re}(u)$ and $\mathrm{Im}(u)$, varies with the phase of $k(x - c_r t)$ but $|u|$ remains constant. The particular phase of u shown here is for a zero phase of $k(x - c_r t)$. The scale for u on the ordinate is arbitrary, and the free streamlines are located initially at $y' = -1$ and $y' = +1$ on the abscissa. A mirror image of this eigenfunction (maximal amplitude at -1) also exists (after Paldor and Ghil 1990).

for this decay is a few kilometers only, which is supported by the observed velocity profile (cf. Fig. 2b).

The PG theory yields a vertical velocity W in the active layer that varies linearly with height z at all times:

$$W = \frac{z}{H}\frac{dh}{dt},$$

where H is the frontal elevation in the basic state, while h is its perturbation height. A vertical profile of W is not available in IOP-4, so that direct confirmation of the linearity of W with z is not possible. Very close to the ground, however, where z is very small, we expect W to be essentially zero, except for the immediate vicinity of the free streamline where z/H is O(1) so that W can attain its maximal value of dh/dt. Such a *horizontal* cross section of W is available and is shown in Fig. 7. It is clear in this observed horizontal cross section that W is essentially zero except very close to the cold front, where its magnitude is comparable to that of dh/dt, as obtained from earlier considerations.

b. Energetics

The increase in the perturbations' total energy, kinetic plus potential, was shown in PG to have two sources: a barotropic one, $HU_y\langle uv\rangle$—proportional to the Reynolds stress term in the active layer—and a baroclinic one, $U\langle\phi_x p\rangle$—due to the phase difference between the upper and lower-layer pressure. Here U is the basic-state velocity in the active layer, u, v are the along- and cross-front perturbation velocities in the active layer, and ϕ, p are the perturbation pressures in the upper and lower layer, respectively. These two sources for the perturbation energy are shown schematically in Fig. 8.

It is clear from the figure that the barotropic term converts the shear of the mean flow into the wave motion of the perturbation, while the baroclinic term extracts perturbation energy out of the quadrature of the upper- and lower-layer pressures. The IOP-4 observations are not sufficiently detailed to permit computing

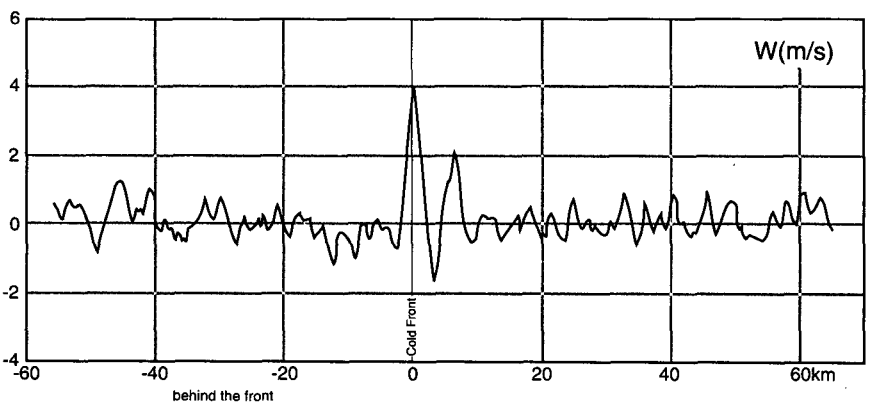

FIG. 7. The horizontal cross section of W (the vertical velocity in the active layer) at a height of 300 m at 0600 UTC. The sharp increase of the vertical velocity right near the free streamline, evident in these observations, is in good agreement with the theoretical behavior of W near $z = 0$ and $y' = +1$.

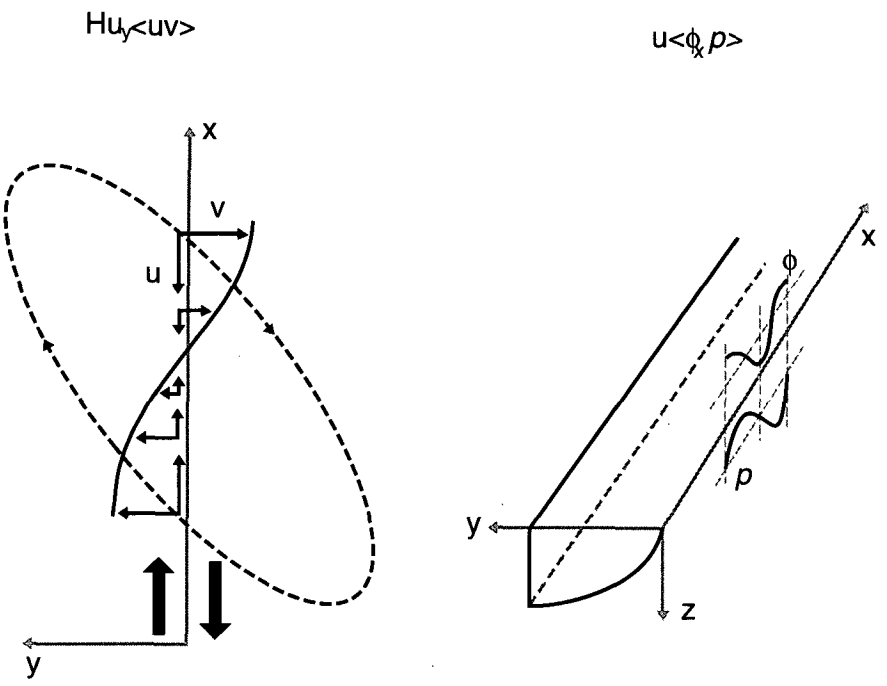

FIG. 8. Schematic diagram of the source terms for the increase in total perturbation energy. Left panel—the barotropic source: H is the height of the active layer and U is the alongfront velocity in the basic state; u and v are the along- and cross-front perturbation velocity components in this layer, respectively. The solid curve outlines the amplitude of both the velocity components in the waves (each shown at a number of along-front positions as solid arrows); the dashed ellipse shows the associated particle motion in the wave; the heavy arrows indicate the alongfront shear in the basic state, $\pm U/2$. Right panel—the baroclinic source: ϕ and p are the perturbation pressures in the active and passive layer, respectively. The two solid curves, drawn for ϕ and p, show the phase relationship between the pressure perturbations in the upper and lower layer, respectively.

these two terms separately. But the schematic diagram here provides a more complete description of the PG instability and of its applicability to short-wave frontal instabilities.

5. Discussion and conclusions

The new frontal instability model of Paldor and Ghil (1990) is shown to be applicable to perturbations along an atmospheric cold front. This theory—while ignoring moisture effects—predicts fairly well the observed growth rates on the ERICA IOP-4 front, based on the dynamics of the frontal flow only. The same theory might also be applicable to some of the observations on so-called wide cold-frontal rainbands reported by Parsons and Hobbs (1983b). Other theories, such as Kelvin–Helmholtz (K–H) instabilities (Mueller and Carbone 1987) or Moore's (1985) moist-convective instability, must be relevant to the much faster growth rates with O(10 min) doubling times observed in certain cases (Carbone 1983; Parsons and Hobbs 1983b).

Our study is also relevant to the ongoing debate regarding the selection mechanism that determines the length scale of the frontal perturbations when the instability spectrum allows for a very broad range of length scales. To begin with, it should be noted that K–H waves were observed on the ERICA front (Wakimoto et al. 1992) as well as on other fronts (e.g., Nielsen 1992 and references therein). These waves have a length scale of 3–5 km, one order of magnitude smaller than the unstable waves reported here.

Given that instabilities with such a wide range of length scales, for example, long- and short-wave PG instabilities as well as the much shorter K–H waves, can develop on a front like ERICA, what determines the wavelength of observed frontal instabilities? The selection issue is related to that of the growth-limiting mechanism for linear instabilities. One such mechanism was advocated by Orlanski and Ross (1984), who found ageostrophic viscous damping by turbulent diffusion to limit the growth by displacing the region of maximum horizontal divergence away from that of maximum vorticity. In the numerical experiments of Gall et al. (1987), on the other hand, the initial growth of the front was eventually stopped even though no dissipation terms were included in their primitive equa-

tion model. The final length scale in the latter simulations was determined by the vertical resolution.

The linear, inviscid PG theory cannot address directly either the selection mechanism or the limiting process; a step in the direction of a comprehensive theoretical treatment of the role of weak nonlinearities in wavelength selection and saturation is made by Ghil and Paldor (1994). On the other hand, the PG theory can be used to assess the actual importance of the viscous terms for the full process. Suppose it were dissipation that balances the temporal growth of the instability. Then, if the dissipation were Laplacian, this balance would require (cf. Paldor and Ghil 1991) that

$$kc_i \sim Ak^2,$$

where A is an eddy viscosity coefficient. In the case of the ERICA front, $k \sim 100$ and $c_i \sim 0.015$; an estimate of the nondimensional value of the dissipation coefficient is $A \approx 2 \times 10^{-4}$ and in dimensional units $A^* = AL^2 f \approx 10^4$ m^2 s^{-1}. This value is a few orders of magnitude larger than any value used for simulating frontal evolution. Thus, it seems that our study supports the findings of Gall et al. (1987); that is, it is not the dissipation that limits the growth of the instabilities.

In support of the application of the PG theory very close to the free streamline, we should mention the analytic study of Holt and Shutts (1990), who convincingly showed that the hydrostatic assumption, on which the PG theory is based, holds—to a very good approximation—at all times. Referring to the vertical-resolution limitation reported by Gall et al. (1987), we conjecture here that the eventual length scale of secondary frontal instabilities is determined by an interaction of the purely dynamic PG instability with convective processes that are absent from the present theory, but might provide the preferred length and eventual amplitude.

It is remarkable that, in spite of the rapid evolution of other instabilities, some features on the ERICA front remained intact for a couple of hours, only to be eventually dissipated by the PG instability. Johnston (1974) has also reported on infrared satellite observations indicating an exponential growth of a frontal wave with an e-folding time of a few hours, but with much larger dimensional wavelength. Unfortunately, no data are available there on the velocity structure or density profile to help determine the cause and nature of the instability, that is, whether it be short wave or long wave.

Acknowledgments. We thank P. J. Neiman and colleagues for the use of the data in Fig. 2, and W. Blier and K. Ide for helpful references. Two anonymous referees helped improve the presentation considerably. This research was supported by ONR Grants N00014-90-J-1602 (NP and MG) and N00014-91-J-1068 (CHL and RMW), by NSF Grant OCE-87-17144 (NP), and by an NSF Special Creativity Award (MG). MG would also like to thank R. Sadourny and the staff of the Laboratoire de Météorologie Dynamique du CNRS, Ecole Normale Supérieure, Paris, for an interesting and stimulating sabbatical (1991–92). The paper was typed by C. Wong and K. E. Mah.

APPENDIX

The Spatial Structure of the Eigenfunctions

The equations for the active layer's downstream perturbation velocity u and passive layer's perturbation pressure p [Eqs. (3.5), (3.6) of PG] can be written as

$$\frac{4}{k^2}[(r-H)p_z]_z = -\left(c^2 - \frac{1}{k^2}\right)(U-c)u - \left[\left(c^2 - \frac{1}{k^2}\right) - (r-H) + \frac{U}{c}\right]p, \quad \text{(A1)}$$

$$\frac{4}{k^2}[Hu_z]_z = [H - (U-c)^2]u - (U-c)p; \quad \text{(A2)}$$

here $-1 \leq z \leq 1$ and $U(z) = z/2$ is the mean downstream velocity in the active layer, while

$$H(z) = (1 - z^2)/8$$

is the mean height of that layer and c is the phase speed of the alongfront waves. The boundary conditions associated with these equations are

$$p_z = \mp \frac{k}{2} p, \quad z = \pm 1, \quad \text{(A3)}$$

$$|u| < \infty, \quad z = \pm 1. \quad \text{(A4)}$$

The last boundary condition for u guarantees the regularity of the u eigenfunction at the singular endpoints, where H vanishes. Local analysis of the regular u solution near these singular points shows that

$$u_z = k^2(U-c)[(U-c)u + p], \quad z = \pm 1,$$

so that the u derivative is $O(k^2)$ near the endpoints.

Assuming u and p are eigenfunctions of the system (A1), (A2) with an eigenvalue c, we can determine the spatial variation of the u eigenfunction in the limit $k \to \infty$ by employing a WKB expansion (Bender and Orszag, 1978) for both u and p:

$$u \sim e^{(1/\delta)\sum_{n=0}^{\infty} \delta^n T_n(z)}, \quad \text{(A5)}$$

$$p \sim \epsilon e^{(1/\delta)\sum_{n=0}^{\infty} \delta^n S_n(z)}. \quad \text{(A6)}$$

Here δ is a small parameter and ϵ is the ratio between the maximal value of p and that of u. Our numerical results (e.g., Fig. 6) have shown that $\epsilon < 1$, due to the singularity of the u equation (A2).

Substituting the expansion (A5), (A6) in Eqs. (A1), (A2), we get

$$\frac{4\epsilon}{k^2}\left\{U\frac{1}{\delta}\sum\delta^n S_n' + (r-H)\left[\frac{1}{\delta^2}\left(\sum\delta^n S_n'\right)^2 + \frac{1}{\delta}\sum\delta^n S_n''\right]\right\}$$

$$= \left(c^2 - \frac{1}{k^2}\right)(U-c)A - \epsilon\left[\left(c^2 - \frac{1}{k^2}\right) - (r-H) + \frac{U}{c}\right], \quad \text{(A7)}$$

$$\frac{4}{k^2}\left\{-U\frac{1}{\delta}\sum\delta^n T_n' + H\left[\frac{1}{\delta^2}\left(\sum\delta^n T_n'\right)^2 + \frac{1}{\delta}\sum\delta^n T_n''\right]\right\} = [H-(U-c)^2] - (U-c)\epsilon A^{-1}, \quad \text{(A8)}$$

where

$$A(z) = e^{(1/\delta)\sum_{n=0}^{\infty}\delta^n(T_n - S_n)}$$

and where the prime denotes differentiation with respect to z. For a consistent scaling we choose $\delta \sim 2/k$ and assume $|U-c| \sim \epsilon$; this too is confirmed by our numerical results.

Under these assumptions, the dominant terms in Eq. (A8) are at O(1)

$$HT_0'^2 = H + O(\epsilon^2), \quad \text{(A9)}$$

and at O(δ)

$$-UT_0' + H(T_1'^2 + T_0'') = 0 + O(\epsilon^2). \quad \text{(A10)}$$

The eikonal equation (A9) yields the solution

$$T_0 \sim \pm z, \quad \text{(A11)}$$

while the transport equation (A10) yields

$$(T_1')^2 = \pm\frac{U}{H} = \pm 4\frac{z}{1-z^2}. \quad \text{(A12)}$$

The zeroth-order solution (A11) demonstrates the exponential decay of u away from the singular end points, $u(z) \sim e^{-|z|k/2}$, which becomes sharper as k increases. The first-order correction to this, Eq. (A12), can be written in terms of elliptic functions of the first kind, by realizing that T_1 satisfies the equation

$$\frac{\partial T_1}{\partial\phi} \sim \sqrt{\sin\phi},$$

where $\phi = \arcsin z$. Thus, T_1 represents the oscillation pattern of the eigenfunctions away from the end points. Our numerical experiments up to $k = 50$, here and elsewhere [see, for instance, Fig. 6 in Paldor and Ghil (1991)], show that the number of nodes also increases with k, although this increase appears only at higher order in the WKB analysis presented here. This increase in the number of nodes is the reason why, at high wavenumbers, the numerical integration of the eigenproblem equations is so sensitive to the precise value of k and c, rendering the numerical calculation of the eigenfunctions impractical. On the other hand, the asymptotic value of c_r shown in Fig. 5 here is slightly less than the value of the mean velocity at the free streamline, which is consistent with the amplitude of the corresponding eigenfunction attaining its maximum at the same streamline.

REFERENCES

Bender, C. M., and S. A. Orszag, 1978: *Advanced Mathematical Methods for Scientists and Engineers,* McGraw-Hill, 484–544.

Carbone, R. E., 1983: A severe frontal rainband. Part II: Tornado parent vortex circulation. *J. Atmos. Sci.*, **40,** 2639–2654.

Gall, R. L., R. T. Williams, and T. L. Clark, 1987: On the minimum scale of surface fronts. *J. Atmos. Sci.*, **44,** 2562–2574.

Ghil, M., and N. Paldor, 1993: Nonlinear wavelength selection and amplitude evolution of frontal waves. *J. Nonlin. Sci.*, in press.

Griffiths, R., P. D. Killworth, and M. E. Stern, 1982: Ageostrophic instability of ocean currents. *J. Fluid Mech.*, **117,** 343–371.

Hadlock, R., and C. W. Kreitzberg, 1988: The experiment of rapidly intensifying cyclones over the Atlantic (ERICA) field study: Objectives and plans. *Bull. Amer. Meteor. Soc.*, **69,** 1309–1320.

Hobbs, P. V., 1978: Organization and structure of cloud and precipitation on the mesoscale and microscale in cyclonic storms. *Rev. Geophys. Space Phys.*, **16,** 741–755.

——, and K. R. Biswas, 1979: The cellular structure of the narrow cold-front rainband. *Quart. J. Roy. Meteor. Soc.*, **105,** 723–727.

——, and P. O. Parsons, 1982: The mesoscale and microscale structure and organization of clouds and precipitation in midlatitude cyclones. Part V: The substructure of narrow cold-frontal rainbands. *J. Atmos. Sci.*, **39,** 280–295.

Holt, M. W., and G. J. Shutts, 1990: An analytical model of the growth of a frontal discontinuity. *Quart. J. Roy. Meteor. Soc.*, **116,** 269–286.

Houze, R. A., and P. V. Hobbs, 1982: Organization and structure of precipitating cloud system. *Advances in Geophysics,* Vol 24, Academic Press, 225–315.

——, ——, K. R. Biswas, and W. M. Davis, 1976: Mesoscale rainbands in extratropical cyclones. *Mon. Wea. Rev.*, **104,** 868–878.

James, P. K., and K. A. Browning, 1979: Mesoscale structure of line convection at surface cold fronts. *Quart. J. Roy. Meteor. Soc.*, **105,** 371–382.

Johnston, E. C., 1974: Rapid frontal wave development. *Mon. Wea. Rev.*, **102,** 804–806.

Moore, G. W. K., 1985: The organization of convection in narrow cold-front rainbands. *J. Atmos. Sci.*, **42,** 1777–1791.

Mueller, C. K., and R. E. Carbone, 1987: Dynamics of a thunderstorm outflow. *J. Atmos. Sci.*, **44,** 1879–1898.

Neiman, P. J., M. A. Shapiro, and L. S. Fedor, 1991: Synoptic and mesoscale frontal characteristics within an intense extratropical marine cyclone: ERICA IOP 4, 4-5 January 1989. Preprints, *First Int. Symp. on Winter Storms,* New Orleans, Amer. Meteor. Soc., 108–114.

——, ——, and ——, 1993: The life cycle of an extratropical marine cyclone. Part II: Mesoscale structure and diagnostics. *Mon. Wea. Rev.*, **121,** 2177–2199.

Nielsen, J. W., 1992: In situ observations of Kelvin–Helmholtz waves along a frontal inversion. *J. Atmos. Sci.*, **49,** 369–386.

Orlanski, I., 1968: Instabilities of frontal waves. *J. Atmos. Sci.*, **25,** 178–200.

——, and B. B. Ross, 1984: The evolution of an observed cold front. Part II: Mesoscale dynamics. *J. Atmos. Sci.*, **41,** 1669–1703.

Paldor, N., 1986: Nonlinear waves on a coupled density front. *Geophys. Astrophys. Fluid Dyn.*, **37,** 171–191.

——, and P. D. Killworth, 1987: Instabilities of a two-layer coupled front. *Deep-Sea Res.*, **34(a),** 1525–1539.

——, and M. Ghil, 1990: Finite-wavelength instability of a coupled density front. *J. Phys. Oceanogr.*, **20,** 114–123.

——, and ——, 1991: Shortwave instabilities of coastal currents. *Geophys. Astrophys. Fluid Dyn.*, **58,** 225–241.

Parsons, D. B., and P. V. Hobbs, 1983a: The mesoscale and microscale structure and organization of clouds and precipitation in midlatitude cyclones. VII: Formation, development, interaction and dissipation of rainbands. *J. Atmos. Sci.*, **40,** 559–579.

——, and ——, 1983b: The mesoscale and microscale structure of clouds and precipitation in midlatitudes cyclones. XI: Comparisons between observational and theoretical aspects of rainbands. *J. Atmos. Sci.*, **40,** 2377–2397.

Shapiro, M. A., and D. Keyser, 1990: Fronts, jet streams and the tropopause. *Extratropical Cyclones: The Erik Palmén Memorial Volume,* T. Malone, Ed., Amer. Meteor. Soc., 167–191.

——, E. G. Donall, P. J. Neiman, L. S. Fedor, and N. Gonzalez, 1991: Recent refinement in the conceptual models of extratropical cyclones. Preprints, *First Int. Symp. on Winter Storms,* New Orleans, Amer. Meteor. Soc., 6–13.

Stone, P. H., 1970: On non-geostrophic baroclinic stability: Part II. *J. Atmos. Sci.*, **27,** 721–726.

Stull, R. B., 1988: *An Introduction to Boundary Layer Meteorology.* Kluwer Academic, 666 pp.

Wakimoto, R. M., W. Blier, and C. Liu, 1992: The frontal structure of an explosive oceanic cyclone: Airborne radar observations of ERICA IOP 4. *Mon. Wea. Rev.*, **120,** 1135–1155.

Wang, P-Y., and P. V. Hobbs, 1983: The mesoscale and microscale structure and organization of clouds and precipitation in midlatitude cyclones. X: Wavelike rainbands in an occlusion. *J. Atmos. Sci.*, **40,** 1950–1964.

——, D. B. Parsons, and P. V. Hobbs, 1983: The mesoscale and microscale structure and organization of clouds and precipitation in midlatitude cyclones. VI: Wavelike rainbands associated with a cold-frontal zone. *J. Atmos. Sci.*, **40,** 543–558.